https://doi.org/10.1016/j.nanoen.2019.01.032

Micropatterned elastic ionic polyacrylamide hydrogel for low-voltage capacitive and organic thin-film transistor pressure sensors

Ming-Jie Yin[a], Zhigang Yin[b], Yangxi Zhang[a], Qingdong Zheng[b,*], A. Ping Zhang[a,*]

[a] Photonics Research Center, Department of Electrical Engineering, The Hong Kong Polytechnic University, Hong Kong SAR, China

[b] State Key Laboratory of Structural Chemistry, Fujian Institute of Research on the Structure of Matter, Chinese Academy of Sciences, 155 Yangqiao West Road, Fuzhou, China.

*Corresponding author
E-mail address: qingdongzheng@fjirsm.ac.cn (Q. Zheng); azhang@polyu.edu.hk (A.P. Zhang).

ABSTRACT

Electronic skins (E-skins) have attracted great research interest because of their promising applications in stretchable optoelectronics, soft robotics, and personalized healthcare devices. However, it remains a great challenge to fabricate E-skin devices that meet strict practical requirements such as high sensitivity, low-power operation and noise-proof ability. Here, we developed a novel elastic ionic polyacrylamide hydrogel (EIPH) with a high capacitance for the development of low-voltage organic thin-film transistor (OTFT) pressure sensors. The EIPH was prepared by photopolymerization of an acrylamide monomer in an aqueous solution of poly (acrylic acid) and $CaCl_2$ and was then *in situ* micropatterned on an indium-tin oxide electrode. The fabricated capacitive sensor with 10-μm-wide EIPH micropillar structures achieved a high sensitivity of 2.33 kPa^{-1} with a capacitance sensitivity of 103.8 nF/kPa. This capacitance sensitivity is more than 100 times higher than that of conventional capacitive pressure sensors due to the formation of an electrical double layer. The micropatterned EIPH was adopted as a dielectric layer in the fabrication of the OTFT-based pressure sensors.

Such an EIPH-based OTFT pressure sensor not only greatly enhanced the sensitivity, i.e., 7.7 times higher than its capacitive counterparts, but also largely reduced the operation voltage to 2 volts.

Keywords

Elastic hydrogel; Capacitive pressure sensors; Organic thin-film transistors; Low-voltage; Electronic skins

1. Introduction

Human skin enables us to perceive the changes in the contact pressure and the shapes and textures of objects. To mimic these abilities, various flexible pressure sensors have been developed [1-5], especially for the applications of electronic skin (E-skin) [6-7], soft robotics [8-9], flexible touch displays [10-13], energy harvesting [14-15], and healthcare [16-20]. The working mechanisms of these pressure sensors include piezoelectricity [20-26], capacitance [11, 16-17, 27-28], triboelectricity [10, 29-30], and piezoresistivity [31-34], in which an applied force is converted into electrical signals that can be directly read. Particularly, capacitive sensors have recently gained enormous success in consumer electronics because of their distinct advantages of high electrical sensitivity, low-power consumption, compact circuit layout, and a simple device fabrication process [35-36]. Substantial advancements have been achieved in recent years, aiming at improving the sensitivity of capacitive pressure sensors to detect ultralow pressure variations [2, 17]. For example, Bao's group proposed to pattern polydimethylsiloxane (PDMS) into microstructures to enhance the sensitivity of PDMS-based pressure sensors [27-28]. Kwon et al. demonstrated a highly sensitive piezocapacitive pressure sensor using a three-dimensional (3D) microporous Ecoflex dielectric layer [17]. However, the sensitivities of those pressure sensors are lower than 1 kPa^{-1}, even in the low-pressure range.

One promising solution to this issue is to further integrate the microengineered elastomer into organic thin-film transistors (OTFTs) for signal amplification and sensing-mechanism diversification [1-3, 37]. Indeed, given by their excellent flexibility, light-weight, and potentially low-cost [38], OTFT devices have been broadly

demonstrated for various flexible sensing applications [39-41]. For instance, an OTFT-based pressure sensor was first proposed by Someya et al. [42], in which an OTFT was employed as an electronic readout element for conductive rubber pressure sensing components. The sensitivity of the sensor, however, is not high due to the limitation of the integrated conductive rubber sensing element. Later, Bao et al. incorporated microstructured PDMS as a dielectric layer into a flexible OTFT-based pressure sensor [5] and achieved a high sensitivity up to 8.2 kPa^{-1} with the ability of subtle pressure detection [18]. More recently, the sensitivity of the OTFT-based pressure sensor was enhanced to an ultrahigh level of 192 kPa^{-1} with well tunability by using a novel suspended gate OTFT structure [19]. Nevertheless, the operation voltage of most OTFT-based pressure sensors is usually high and ranges from tens to even hundreds of volts [5, 18-19], which limits their practical application particularly in portable and wearable electronic devices.

Enhancing the capacitance of the dielectric layer is a well-proved way to reduce the operation voltage of OTFT devices [43]. Notably, the ionic materials, consisting of a substantial number of mobile cations and anions, can form an electrical double layer (EDL) with exceptionally high unit area capacitance, once sandwiched between two electrodes [35, 44-46]. The capacitances of the ionic materials are typically more than 1000 times greater than that of traditional parallel-plate devices [35-36, 47-50]. Recently, Chang's group utilized an ionic liquid as the electrode to form an EDL structure and then adopted PDMS as an elastomer to fabricate an EDL-based capacitive pressure sensor [49-50]. The sensor revealed a high-pressure sensitivity of 9.55 kPa^{-1}. However, the high sensitivity was only maintained in very narrow pressure range, i.e., from 0 to 0.2 kPa, and its capacitance was not high because of the utilization of PDMS for the dielectric layer. Pan's group demonstrated an EDL-based capacitive pressure sensor by adhering an iontronic film on a flexible electrode and then suspending it upon another flexible electrode [36, 47]. Such a flexible sensor attained a sensitivity of 3.1 nF/kPa. They also reported an EDL-based iontronic microdroplet array device for capacitive pressure sensing, whose sensitivity is relatively lower, i.e. 0.43 nF/kPa [51]. For those dielectric materials, the nonlinear response and complex structure limit their

application for further development of OTFT devices. By mimicking Piezo2 protein in Merkel cells, Kim's group patterned ionic elastomer (ionic-liquid-loaded ionic thermoplastic polyurethane) into pillar-shapes and fabricated a high-performance capacitive sensor covering a wide range of pressures [52-53]. Recently, we demonstrated an EDL-type suspended gate OTFT pressure sensor, in which a polyelectrolyte composite was used to prepare the dielectric layer of the flexible OTFT [48]. The operation voltage of this OTFT sensor is 5 V. However, the fabrication of this type of sensor with dual-layer dielectric layer is sophisticated, and there is still space to further lower the operation voltage because of the low dielectric constant of air.

Inspired by the studies of Suo's group who developed an elastic polyacrylamide (PAAm) composite hydrogel [54], a large number of studies have adopted elastic hydrogels for tactile sensing devices fabrication [12-13, 55-59]. However, no report exists regarding the utilization of an elastic hydrogel as a dielectric layer for capacitive or OTFT-based pressure sensing device development, which may have the potential to enhance the performance of hydrogel-based capacitive pressure sensors. Here, we present a photocrosslinkable elastic ionic polyacrylamide hydrogel (EIPH) to fabricate high-sensitivity low-power-consumption capacitive and OTFT pressure sensors. An in-house digital ultraviolet (UV) lithography technology is applied to *in situ* engineer the EIPH, by precisely controlling the photopolymerization and optically patterning the hydrogel in micrometer scale, on an electrode for direct printing of capacitive pressure sensors. Such capacitive pressure sensors show extraordinarily high sensitivity, long-time stability and a good noise-proof property. Moreover, the micropatterned EIPH can be adopted in an OTFT as a dielectric layer for the fabrication of pressure sensors. Experimental results show that such EIPH-based OTFT sensors not only have extraordinarily high sensitivity but also exhibit a low operation voltage.

2. Material and methods

2.1. Materials

Acrylamide, N,N-methylenebisacrylamide (MBA), 2-hydroxy-4′-(2-hydroxyethoxy)-2-methylpropiophenone (Irgacure 2959), and poly(acrylic acid) (PAA, *Mw*=100 000 g mol^{-1}, 35 wt% aqueous solution) were purchased from Sigma-Aldrich. Poly[4,8-bis(5-(2-ethylhexyl)thiophen-2-yl)benzo[1,2-b;4,5-b']dithiophene-2,6-diyl-alt-(4-(2-ethylhexyl)-3-fluorothieno[3,4-b]thiophene-)-2-carboxylate-2-6-diyl)] (PTB7-Th) was obtained from 1-Material Inc. Poly(indacenodithiophene-co-benzothiadiazole) (PIDT-BT) and tetracyanoquinodimethane (TCNQ) were purchased from Derthon Optoelectronic Materials Science Technology Co., Ltd. and J&K Scientific Ltd. (Beijing), respectively. All the materials were used as received. Other reagents and raw materials were commercially obtained by Sigma-Aldrich Inc., or Adamas-beta Ltd., and were used without further purification. Deionized (DI) water with a resistance of 18 MΩ cm was used in all experiments.

2.2. Micropatternable PAAm solution preparation

Acrylamide monomer (1.8 g) was dissolved in 2.3 g of DI water. Then, 0.26 g of PAA, 0.1 g of Irgacure 2959 (photoinitiator), 0.0072 g of MBA (crosslinker), and 0.0125 g of $CaCl_2$ were added stepwise until fully dissolved under stirring. The prepared photoresist solution was stored for use.

2.3. Capacitive pressure sensor fabrication

The ITO/polyethylene terephthalate (PET) electrode with a thickness of 125 μm was cleaned in an ultrasonic cleaner by immersion into the following solvents: acetone, water, and isopropyl alcohol, each for 30 min. The electrode was then blow dried with a nitrogen gun. The photoresist solution was dropped on the ITO/PET electrode and micropatterned with an in-house optical maskless exposure setup *via* UV light (365 nm). The intensity of the UV light was 15.65 mW/cm^2, and the exposure time was 40 s. After the patterning process, the micropatterned EIPH (area: 1 cm^2) was laminated with another ITO/PET electrode to prepare the capacitive pressure sensors. Then, the sensors were photoannealed by an 8 W UV light for 30 min to reach the desired elasticity.

2.4. OTFT-based pressure sensor fabrication

All the OTFT pressure sensors were prepared on 175-μm-thick PET. After cleaning this plastic substrate, 50-nm-thick gold (Au) as the source/drain (S/D) electrodes was deposited on top of PET by thermal evaporation *via* a shadow mask with a channel width and length of 22.5 mm and 0.15 mm (W/L=150), respectively. This evaporation process was performed under a high vacuum (~2×10^{-4} Pa), and the evaporation rate for Au was approximately 0.5 Å/s. Prior to the semiconductor deposition, the Au S/D electrodes on the PET substrates were treated with UV-O_3 for 15 min and then transferred into a nitrogen-filled glovebox. Thereafter, the organic semiconductor layer was fabricated by spin-casting (2000 rpm, 60 s) a PTB7-Th solution (dissolved in chlorobenzene with a concentration of 3 mg/mL) or a blend PIDT-BT:TCNQ solution (PIDT-BT:TCNQ=49:1 by weight dissolved in chlorobenzene with a total concentration of 5 mg/ml) on the PET/Au surface, followed by annealing at 80 °C for 20 min. Subsequently, a thin PAA protective layer was prepared on the semiconductor layer. Then, the device was again thermally treated at 80 °C for 20 min. The micropatterned PAAm composite hydrogel was also prepared on the ITO-coated PET following the same procedure described above. Finally, this flexible gate/dielectric part was laminated under ambient conditions by pressing the electrodes against each other and fixing by tape in the device.

2.5. Characterizations and device tests

The microstructures of PAAm composite hydrogels were measured by 3D laser scanning confocal microscope (VK-X200, KEYENCE, Japan) and scanning electron microscopy (JEOL Model JSM-6490). The former is a non-contact laser scanning imaging machine. The magnification of the objective lens used for scanning was 50×.

Fourier-transform infrared spectroscopy (FTIR) spectra were recorded by a Bruker Vector Spectrometer (Tensor II). The compressive stress–strain measurements were performed using a tensile-compressive tester (Instron-5942 with a 500 N sensor) in air. The rate of compression was kept constant as 2% s^{-1} with respect to the original height of the hydrogel, roughly 5 mm min^{-1}.

The capacitances were measured by LCR-819 (GW Instek, Taiwan, 12 Hz-100 kHz, with accuracy of 0.5%) with an applied voltage of 0.1 V. The electrical characteristics of all the OTFT pressure sensors were measured in ambient air by using an Agilent 4155C semiconductor parameter analyser. The force applied on the sensors was precisely controlled with a force gauge (Model No.: JSV-H1000).

3. Results and discussion

Fig. 1a shows the scheme of the photopolymerization process to prepare the EIPH with UV light. Specifically, monomers of acrylamide are photopolymerized with a photoinitiator (Irgacure 2959) and crosslinked by the crosslinker (N,N-methylenebisacrylamide, MBA) *via* radical polymerization [59-60], which leads to the formation of 3D networks through covalent bonds. Meanwhile, the PAAm chains will interact with poly(acrylic acid) (PAA) *via* hydrogen bonds, thereby forming a double-network hydrogel. Moreover, the PAA chains are simultaneously crosslinked by Ca^{2+} *via* electrostatic forces (i.e., ionic bonds), which can further enhance the mechanical strength of the composite hydrogel [59]. Such an EIPH with the three kinds of bonding forces is shown in Fig.1b. Notably, the ionic bonds and hydrogen bonds in the EIPH can dynamically break/form during the process of applying/releasing pressure along with energy dissipation [54, 58-59]. Particularly, the covalent crosslinked PAAm networks play an essential role in maintaining the initial geometry of the 3D hydrogel structure, while the ionic bonds and hydrogen bonds render the superelasticity of the EIPH. Fig. S1 gives the FTIR spectra of EIPH, PAA and PAAm hydrogel. The peak located at 1702 cm^{-1} is the typical carbonyl group of PAA [61]. For PAAm hydrogel, the peak at 1655 cm^{-1} and the shoulder at 1605 cm^{-1} are corresponding to the C=O vibrations of the amide group and the primary amine N-H deformation vibrations, respectively [62]. However, those peaks show redshift in the spectrum of EIPH, and the peak for hydroxide stretching mode and the ─NH stretching mode becomes wider in EIPH, compared with PAAm hydrogel, which indicates the formation of hydrogen bonding in the EIPH [63].

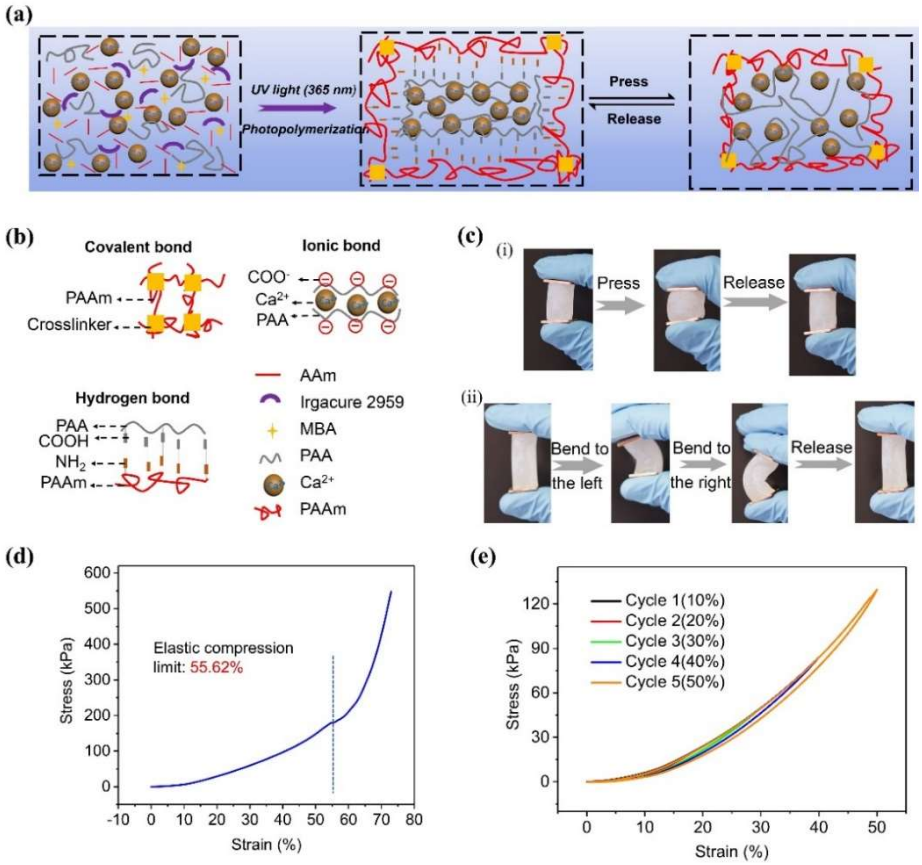

Fig. 1. Photopolymerization and elastic property of the EIPH. (a) Schematic of the photopolymerization process and the reversible breaking/forming of secondary bonds with/without pressure. (b) Three kinds of bonds in the EIPH: covalent bonds between PAAm, ionic bonds between PAA and Ca^{2+}, and hydrogen bonds between PAAm and PAA. (c) Demonstration of the highly elastic property of the EIPH under pressing (top panel) and bending (bottom panel) conditions. (d) The elastic compression limit of EIPH. (e) The measured stress–strain curves of the EIPH with the cycles of the reversible strain changes from 0 to 10%, 20 %, 30 %, 40%, and 50%, respectively.

In Fig. 1c, the EIPH can be flexibly bent or highly pressed and then recovers to its original shape. The EIPH is therefore an ideal material for capacitive pressure sensors because of its superior elastic property as well as good ionic conductivity [56, 64-65]. The mechanical properties of the EIPH were also measured, as shown in Fig. 1d and Fig. 1e. The compression limit is an important parameter, which determines the pressure sensing range of the fabricated sensor. Fig. 1d shows the tests of elastic compression ability of EIPH. The stress shows nearly linear increase with strain up to 55.64% and a jump with still pressing, which indicates the elastic compression of EIPH is 55.64%. Furthermore, it can be seen in Fig. 1e, the strain response of EIPH to pressure

is reversible and only a little hysteresis between the compression and relaxation traces is observed in five cycles with 10% strain increasing in each cycle, suggesting the great capability of the EIPH for pressure sensing. Also, the compression Young's modulus can be calculated as 90.14 kPa and 329.2 kPa in the strain range of 0 ~10 % and 20 ~ 40 %, respectively.

Since microstructure plays an important role in elastomer-based pressure sensors [5, 18, 28, 59], the photopatternable property of the EIPH on a flexible substrate of PET coated with indium-tin oxide (ITO) layer was investigated by using an in-house UV digital lithography technology [59-60]. Fig. 2 shows the laser scanning confocal images of the patterned EIPH micropillar structures with widths of 10, 20, 40, and 80 µm. The fabricated EIPH micropillars are regular and uniform across the whole flexible substrate. A uniform structure is essential for the large-area capacitive pressure sensor to provide a clearly defined and reproducible top contact plane [5]. The thicknesses of the hydrogel films are around 45 µm, and more geometric details of the microstructures are given in Fig. S2. SEM images are also provided in Fig. S3. Notably, the EIPH micropillar structures were quickly optically patterned in 40 s. Therefore, such a photopatternable hydrogel is appealing not only for microscale device fabrication but also for large-scale production.

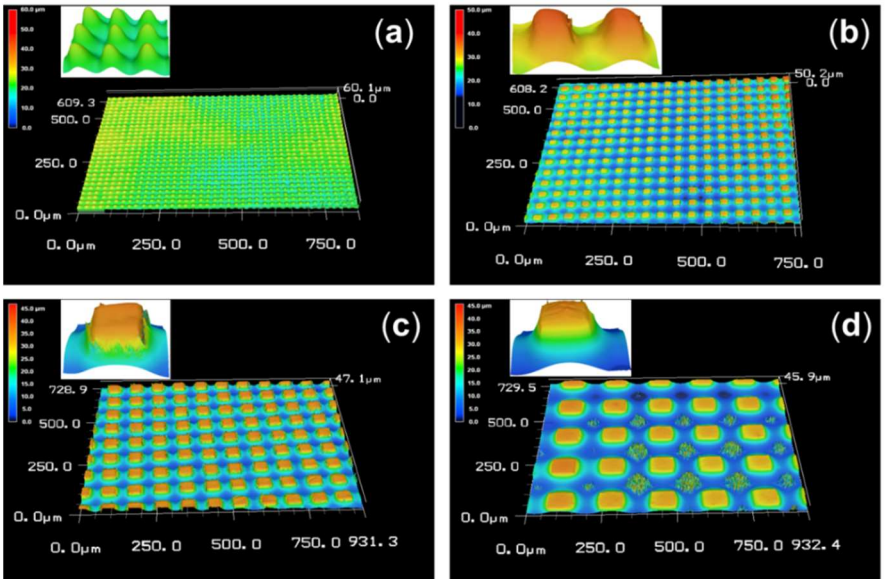

Fig. 2. Laser scanning confocal images of the fabricated EIPH micropillars with different sizes: (a) 10 µm; (b) 20 µm; (c) 40 µm; and (d) 80 µm. The inset shows the enlarged microstructures (both the size and pitch are the same).

The micropatterned EIPH on ITO/PET was then laminated with another flexible ITO/PET substrate to form a capacitive pressure sensor of parallel-plate configuration. The schematic of such an EIPH-based pressure sensor is shown in Fig. 3a. When a voltage is applied, an EDL is generated in the EIPH, which gives rise to the high capacitance of the sensor. With a pressure applied on the sensor, the micropillar EIPH structures deform, which causes an increase in the contact area between the electrodes [5, 18, 59]. As a result, the capacitance of the sensor will increase in accordance with the applied pressure as more charges accumulating at the interface between the electrode and hydrogel [35-36, 47, 66]. In the experiments, four microstructured EIPH-based capacitive pressure sensors were fabricated and are referred to as sensor-1, sensor-2, sensor-3, and sensor-4, whose micropillars have widths of 80, 40, 20, and 10 μm, respectively. In addition, a bulk EIPH-based capacitive pressure sensor, denoted by sensor-0, was also prepared for comparison. The sensors were then tested by using a force gauge mounted on a stepping motor, and the measurement frequency of the tests was 1 kHz.

Fig. 3b summarizes the measured responses of the four microstructured EIPH-based capacitive pressure sensors. Three or more parallel samples were tested for each type of devices. Here, the sensitivity (S) is defined as $S=(\Delta C/C_0)/\Delta P$, where ΔC is the relative change in the capacitance, C_0 is the initial capacitance of the sensor, and ΔP is a change in the applied pressure. It can be seen that the responses of the microstructured EIPH-based sensors show similar responsive behaviours; i.e., the sensor reveals a linear response with high sensitivity when the applied pressure is low (not higher than 3 ~ 3.5 kPa) and then becomes less sensitive when the pressure is further increased. The high sensitivity in the low-pressure range is due to the microstructurally enhanced elastic deformation, which substantially increases the contact area between the EIPH and ITO electrodes and thereby allows more ions in the EIPH to accumulate around the interface, resulting in a high capacitance [35-36]. For the high-pressure range, the elastic resistance of the EIPH increases because of the breaking of ionic bonds and hydrogen bonds as well as the decrease in the microstructure-induced deformation, which

consequently leads to a lower sensitivity [5, 18, 59].

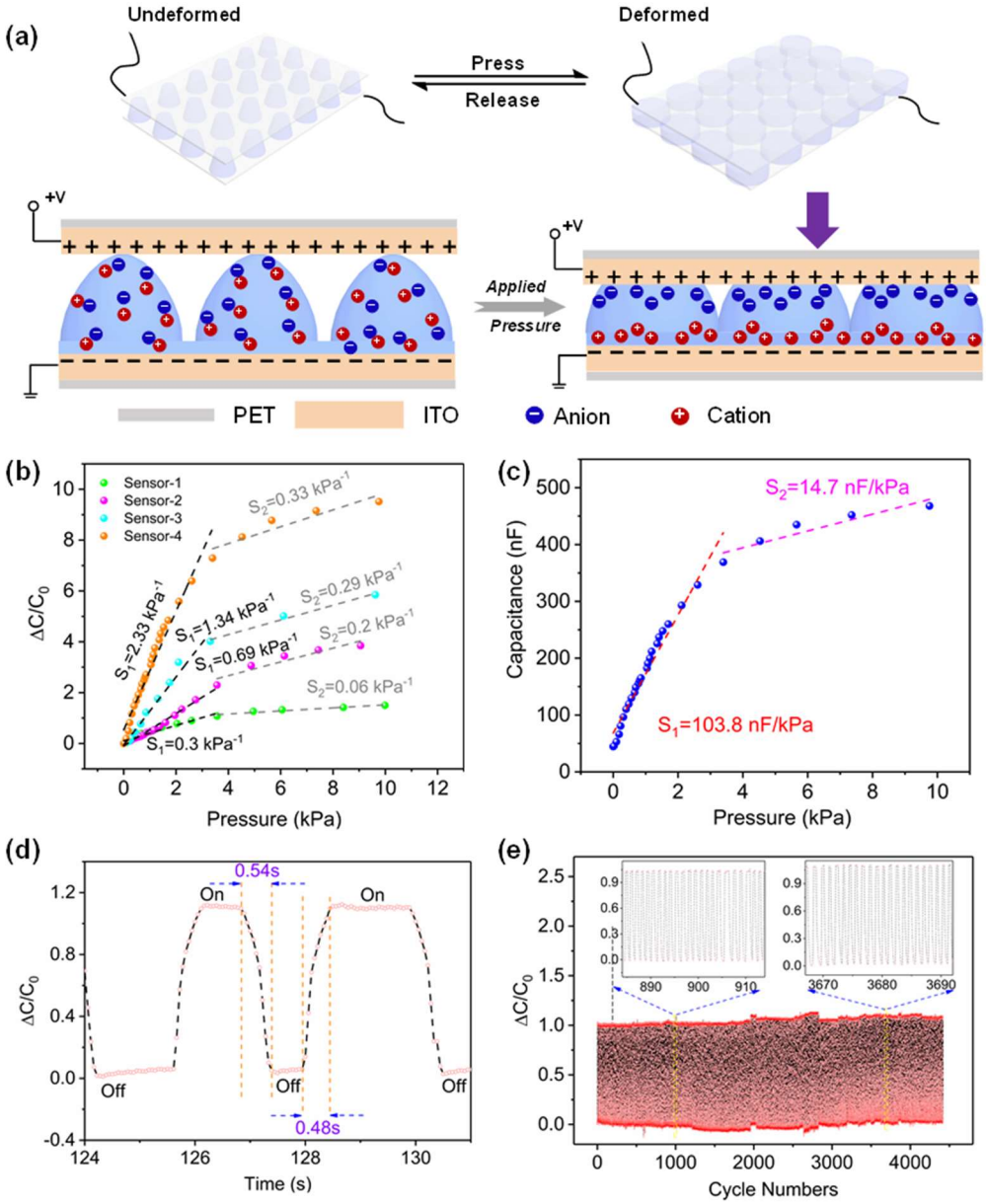

Fig. 3. Schematic and performance of the EIPH-based capacitive pressure sensor: (a) Schematic of the micropatterned EIPH-based capacitive pressure sensor. The top is the shape of the microstructure change with pressure; the bottom is the charge distribution variation in the different states. (b) Pressure-response curves of the pressure sensors with different EIPH microstructures. (c) Capacitance change in the sensor-4 with respect to the applied pressure. (d) Response time of the sensor-4 when the load pressure is 500 Pa. (e) Long-term stability testing result of the sensor-4 under loading/unloading at a pressure of 500 Pa for more than 4, 000 cycles.

Notably, sensor-4 shows the highest sensitivity of 2.33 kPa^{-1} with a detection range up to 3 kPa, which is among top-quality capacitive pressure sensors. The capacitance

of sensor-4 as a function of the applied pressure is provided in Fig. 3c, while the capacitance responses of all other pressure sensors (with micropillar structures) are given in Fig. S4. It can be seen that the sensitivity of sensor-4 is 103.8 nF/kPa in the pressure range of 0-3 kPa, which is hundreds of times higher than that of conventional capacitive sensors [18, 36]. The high-capacitance response is attributed to the large number of ions in the polymer matrix which greatly enhance the capacitance of dielectric layer to nF level (Fig. S4). Moreover, the microstructures enable large change of contact area which further amplify the change of capacitance under pressure. One advantage of the pressure sensor is that it can suppress the adverse influence of the body capacitance (up to hundreds of pF) [35] and other parasitic sources of noise and considerably enhance the measurement accuracy. Besides, the large capacitance would also reduce the operation voltage of OTFT device, lowering the energy consumption of OTFT-based pressure sensors [48, 53]. It indicates the great promise of the sensor for wearable devices applications.

Moreover, the dynamic response of sensor-4 was measured by rapidly loading/unloading a pressure of 500 Pa. In Fig. 3d, the response and relaxation time of sensor-4 are similar: 0.54 and 0.48 s, respectively. The relatively slow response can be attributed to the viscoelastic property of the double-network hydrogel [59, 67]. It can be anticipated that the response of the sensor will further slow down a little bit in the high-pressure range because of the increased elastic resistance of the EIPH. Although the response is not fast, it can still be sufficient in many practical applications, such as detection of human motion [68], measuring wrist pulse of human [69], E-hand skin [59], and so on. The durability of the pressure sensor was tested with repeated loading/unloading at a pressure of 500 Pa for more than 4, 000 cycles, as shown in Fig. 3e. The results indicate that the sensor is stable and shows very little change during the long-time tests.

The effect of bending on the performance of Sensor-4 was also investigated. As shown in Fig. S5, the capacitance of Sensor-4 decreases with the reduction of bending radius. The phenomenon may result from the increase of the distance between microstructures with bending, which reduces the contact area. Notably, the capacitance

of the sensor can almost be recovered when the bending radius is not very small (bending radius > 6 mm). Even if the bending radius is as small as 1 mm, the capacitance of the sensor can be recovered to 70 % of its original value without bending. The result indicates the good potential of the sensor for wearable devices applications. With the decrease of bending radius, the sensitivity of the pressure sensor decreases a bit in the low-pressure range but increases slightly in the high-pressure range, and meanwhile the range of high-sensitivity region increased a little (Fig. S5c-e). It results from the tilt of micropillars which may require higher pressure to reach the same contact area change and allow more space for deformation under press, as illustrated in Fig. S5b.

Besides, the influence of humidity on the capacitance of the sensor was measured, as shown in Fig. S6. The capacitance of the sensor decreased with the increase of humidity, which appeared a nearly linear variation with respect to the humidity ranging from 35% to 70%. It may result from swelling of the EIPH with the increase of humidity. The swelling of the EIPH led to the thickness increase, which thus reduced the capacitance of the sensor. Moreover, the distance between micropillars may decrease with the swelling of the EIPH, which thereby reduces the sensitivity of the sensor [5, 18, 59]. Moreover, the swelling degree of EIPH increases with the temperature in a normal temperature region [70], which thus results in the decrease of sensitivity with the increase of environmental temperature.

With its high capacitance and distinguished elasticity, the micropatterned EIPH was thus further adopted as a pressure-sensitive dielectric layer for OTFT-based pressure sensors. Fig. 4a shows the layout of the OTFT-based pressure sensor. In the device, Au source/drain electrodes were deposited on a PET substrate on which an organic semiconductor (OSC) layer (two kinds of OSCs were used here, as shown in Fig. 4b) was deposited *via* spin-coating. Another part employed an ITO/PET film as a gate electrode, on which EIPH was micropatterned. The two parts were then laminated to form the OTFT sensor.

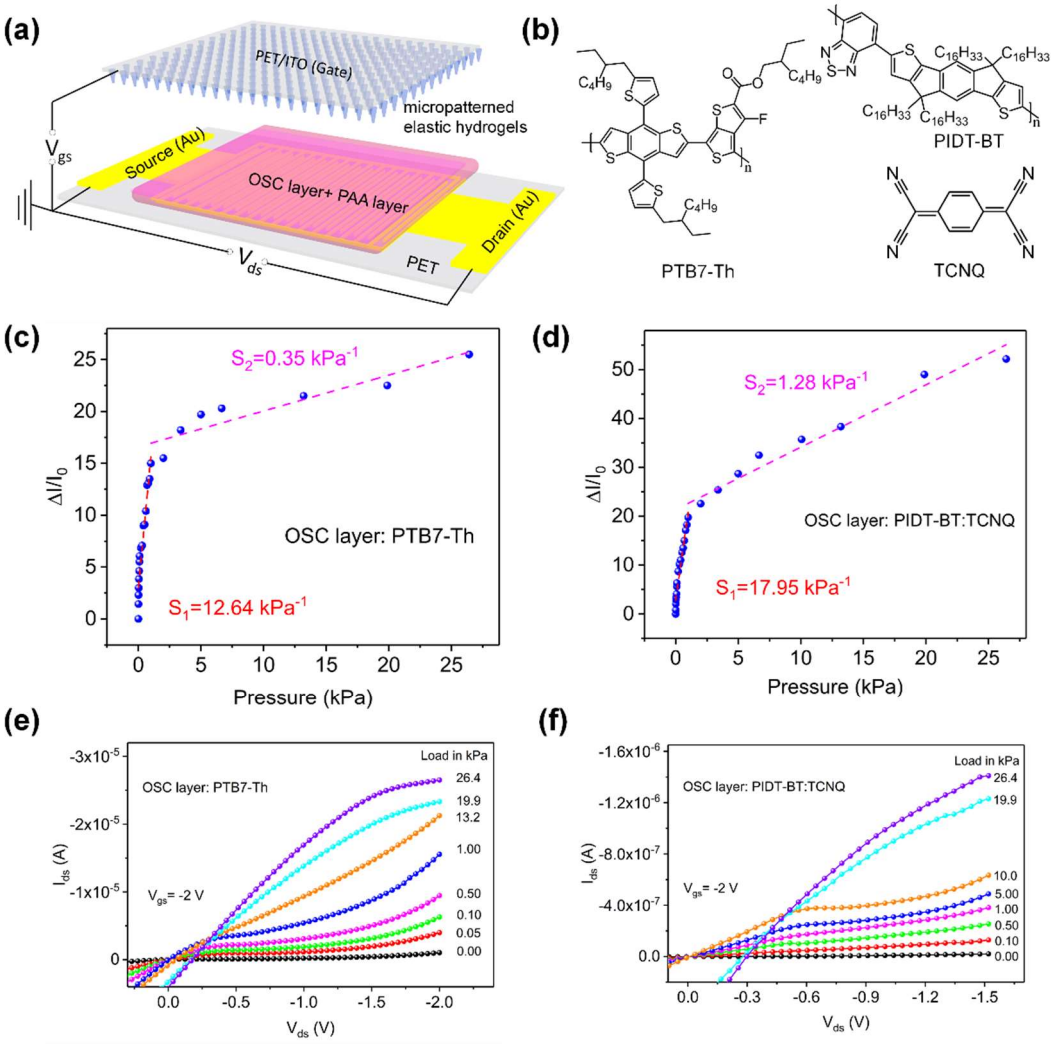

Fig. 4. Schematic and performance of the EIPH-based OTFT pressure sensors: (a) Schematic of the EIPH-based OTFT, consisting of polymer organic semiconductors and a micropatterned EIPH dielectric layer; (b) chemical structures of the organic semiconductors used in OTFT; (c) and (d) saturated current responses of the two OTFT pressure sensors with the OSC layers of PTB7-Th and PIDT-BT:TCNQ; (e) and (f) are the corresponding output drain currents under different pressures.

Fig. 4c and Fig. 4d show the source-drain current (I_{ds}) responses of two p-type OTFT devices, whose OSC layers are PTB7-Th and PIDT-BT:TCNQ, respectively, to the external pressure. The sensitivity of the OTFT-based pressure sensors is defined as $S=(\Delta I/I_0)/\Delta P$, where ΔI is the relative change in the current and I_0 is the initial current of the sensor without pressure loading. Importantly, the sensitivities of the OTFT pressure sensors based on PTB7-Th and PIDT-BT:TCNQ are dramatically enhanced to 12.64 and 17.95 kPa^{-1}, respectively. The improvement in the sensitivities originates

from the signal amplification function of the OTFT [37]. The I_{ds} of OTFT device in saturation region can be calculated from the equation [53]: $I_{ds} = \frac{C\mu W}{2L}(V_g - V_{th})^2$, where I_{ds} is the source-drain current in the saturated region, C is the capacitance of the gate dielectric layer, μ is the field effect mobility, W and L are the semiconductor channel width and length, respectively, V_g and V_{th} are the gate voltage and the threshold voltage, respectively. Thus, it can be clearly seen that the value of I_{ds} is proportional to the capacitance of the gate dielectric layer and hence depends on the applied pressure [5, 18]. Besides, with the sensitivity of 17.95 kPa^{-1}, the minimum detectable pressure can be estimated to be 0.18 Pa at a signal-to-noise ratio of 3. The remarkably high sensitivity of OTFT pressure sensors may resort to two respects: 1) micropatterned EIPH leads to the large change of capacitance of dielectric layer; 2) the formation of EDL which depends on the contact area of dielectric layer and semiconductor layer remarkably modulates the hole generation of semiconductor channel [53]. Notably, the sensitivities of the two OTFT-based pressure sensors are not the same, which can be attributed to the hole mobility variation with the change between the dielectric layer and semiconductor [71]. In addition, a similar phenomenon was also observed in previous OTFT-based pressure sensors [19]. Moreover, the output I_{ds} closely depends on the hole mobility of the OSC layer. It can be seen I_{ds} in Fig. 4e is one order of magnitude larger than that in Fig. 4f, which indicates the much higher mobility of PTB7-Th than that of PIDT-BT:TCNQ (the output curves of two OTFT-based pressure sensors with and without applying pressures were supplied in Fig. S8).

Table 1 summarizes our results as well as some similar OTFT-based pressure sensors whose dielectric layer is an elastic polymer. Compared to other similar OTFT-based pressure sensors, the pressure sensors in our study not only exhibit higher sensitivities but also demonstrate a much lower operation voltage. Our OTFT-based pressure sensors can operate stably at the bias voltages as low as 2 V due to the large capacitance of the EIPH [35-36, 66], which makes them promising for integration into various microdevices for portable and wearable electronics. In addition, compared with previous OTFT-based pressure sensors whose operating voltages are tens or hundreds

of volts, the operating voltage in this work is much lower (Table 1) [5, 18-19, 42].

Table 1 Comparison of the present pressure sensor with previously reported elastic polymer-based capacitive sensors.

Types of Transduction	Materials	Sensitivity (kPa^{-1}) (Sensitivity Region)	Operating Voltage (V)	Ref.
Capacitance	Ecoflex (porous)	0.601 (0-5 kPa)	-	[17]
Capacitance	PDMS (porous)	0.26 (0-0.33 kPa)	-	[16]
Capacitance	PDMS (microstructure)	0.55 (0-2 kPa)	-	[5]
Capacitance	PDMS (microstructure)	0.76 (0-2 kPa)	-	[28]
Capacitance	PDMS	0.00023 (0-900 kPa)	-	[11]
Capacitance	PAAm (microstructure)	2.33 (0-3 kPa)	-	This work
OTFT	PDMS (microstructure) /PiI2T-Si	8.2 (0-8 kPa)	200	[18]
OTFT	Polyurethane (nanostructure)	1.76 (0-1 kPa)	50	[72]
OTFT	(PMMA/PAA)/PIDT-BT:TCNQ	56.15 (0-5 kPa)	5	[48]
OTFT	PAAm (microstructure) /PTB7-Th	12.64 (0-1.5 kPa)	2	This work
OTFT	PAAm (microstructure) /PIDT-BT:TCNQ	17.95 (0-1.5 kPa)	2	This work

To demonstrate the ability of the EIPH-based pressure sensors for tactile sensing applications, we fabricated a proof-of-concept capacitive matrix-type pressure sensor by laminating the micropatterned EIPH-coated ITO/PET substrate with a 4×4 electrode array, as shown in Fig. 5a. The area of each pixel is 49 mm^2. Three objects, made from polystyrene, of different characters such as 'O' and 'K' were used for testing. The objects were placed on the top of the sensor arrays and the induced change in capacitance at each pixel was recorded. Fig. 5(b-d) show the measured response of the sensor array to the placement of these objects, where a greener color represents a larger capacitance. The spillover of the signals from an addressed pixel into a neighboring pixel can be seen and can be improved using smaller pixels. The differences in the color intensity originated from the uneven surface, i.e., the texture structure, of the object. The sensor array shows great potential for multitouch devices.

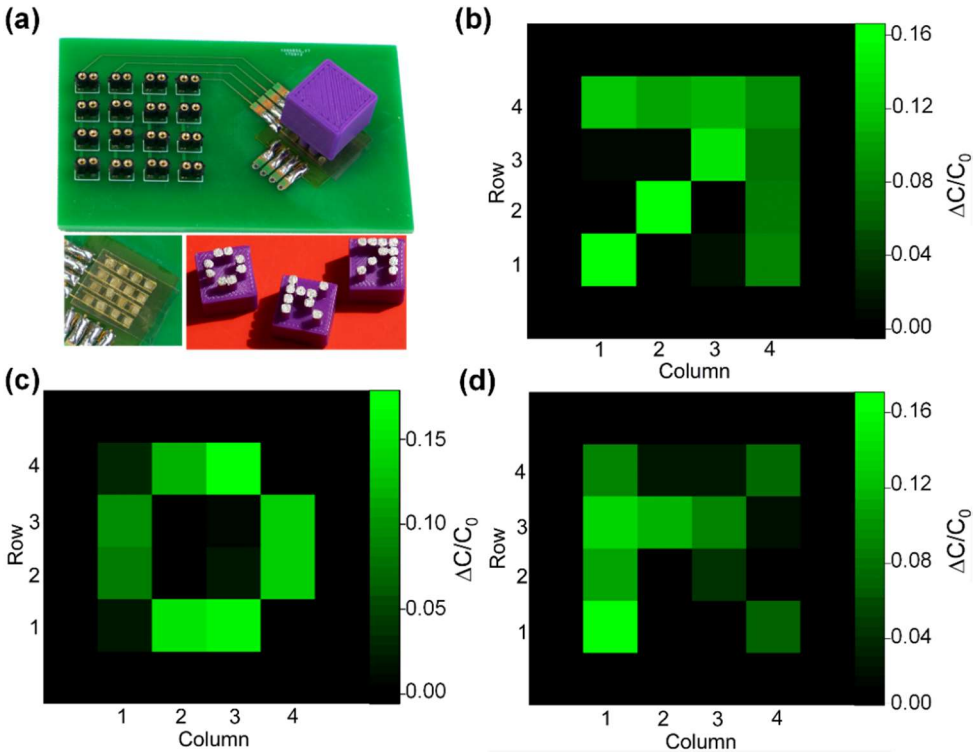

Fig. 5. Demonstration of pressure mapping using the EIPH-based capacitive sensor array: (a) Photos of capacitive matrix-type pressure sensor and the plastic objects with different textures; the response of the device to the placement of objects with different textures: arrow shape (b); O shape (c); and K shape (d).

It is known that microstructures play a key role in improving the sensitivities of pressure sensors [5, 18, 50, 59]. Indeed, compared with the response of the sensor-0 based on the EIPH film without microstructures, as shown in Fig. S9, the sensitivities of pressure sensors with micropillar structures are much higher. In general, the improved sensitivity is due to the micropillar structures that provide more spaces for hydrogel deformation, i.e., the micropillar structures reduce the elastic resistance [5].

Moreover, the geometrical parameters of the microstructures also considerably influence the performance of the pressure sensors. In Fig. 3b., the sensitivities of the microstructured EIPH pressure sensors decrease with an increase in micropillar size. This behavior can be attributed to the following two factors: 1) the effect of smaller micropillars is more significant in the microstructure-enhanced elastic deformation; 2) the contact area between the upper electrode and EIPH hydrogel also depends on the sizes of micropillars, which determines the variation in the capacitance. The former effect has been reported previously [5]. The latter effect can be proven by estimating the initial contact area of the four sensors from Fig. S2. The results are summarized in Fig. S10, which are 0.16, 0.21, 0.31, and 0.42 mm^2 for sensor-4, sensor-3, sensor-2, and sensor-1, respectively, within the fixed probe area of 1.77 mm^2. It can be logically interfered that the smaller initial contact area will provide much more space change. With an applied pressure, a change in contact area leads to a dramatic change in capacitance as the capacitance of an EDL structure depends on the contact area with electrodes [35, 49-50].

4. Conclusion

In summary, we designed and prepared a novel type of elastic ionic hydrogel with high capacitance, i.e., EIPH, by photopolymerization of an acrylamide monomer in an aqueous solution of poly (acrylic acid) and $CaCl_2$. The EIPH was *in situ* micropatterned on an ITO electrode and laminated with another electrode to fabricate capacitive pressure sensors. Because the high elasticity and capacitance of these sensors, the capacitance sensitivity achieved in this work is more than 100 times larger than that of conventional capacitive pressure sensors, which suggests top-quality capacitive

pressure sensors. With the pressure-sensitive property and high capacitance, the micropatterned EIPH was adopted for the first time as a dielectric layer for the fabrication of OTFT-based pressure sensors, which further improved the sensitivity to 17.95 kPa^{-1} with an operation voltage as low as 2 V. The high sensitivity and low-power operation of these flexible capacitive and OTFT pressure sensors render them promising for applications in wearable devices.

Acknowledgments

This work was partially supported by the NSFC/RGC Joint Research Scheme (Grant No.: N_PolyU517/15) and the National Natural Science Foundation of China (No.: 51561165011). Q. Zheng is thankful for the support from the Key Research Program of Frontier Sciences, CAS (No.: QYZDB-SSW-SLH032) and the Strategic Priority Research Program of the Chinese Academy of Sciences (Grant No.: XDB20000000).

References

[1] M.L. Hammock, A. Chortos, B.C.K. Tee, J.B.H. Tok, Z. Bao, Adv. Mater. 25 (2013) 5997-6038.

[2] Y. Zang, F. Zhang, C.-a. Di, D. Zhu, Mater. Horiz. 2 (2015) 140-156.

[3] A. Chortos, Z. Bao, Mater. Today 17 (2014) 321-331.

[4] A. Chortos, J. Liu, Z. Bao, Nat. Mater. 15 (2016) 937-950.

[5] S.C.B. Mannsfeld, B.C.K. Tee, R.M. Stoltenberg, C.V.H.H. Chen, S. Barman, B.V.O. Muir, A.N. Sokolov, C. Reese, Z. Bao, Nat. Mater. 9 (2010) 859-864.

[6] X. Wang, L. Dong, H. Zhang, R. Yu, C. Pan, Z.L. Wang, Adv. Sci. 2 (2015) 1500169.

[7] C. Wang, D. Hwang, Z. Yu, K. Takei, J. Park, T. Chen, B. Ma, A. Javey, Nat. Mater. 12 (2013) 899-904.

[8] S. Bauer, S. Bauer-Gogonea, I. Graz, M. Kaltenbrunner, C. Keplinger, R. Schwödiauer, Adv. Mater. 26 (2014) 149-162.

[9] J. Kim, M. Lee, H.J. Shim, R. Ghaffari, H.R. Cho, D. Son, Y.H. Jung, M. Soh, C. Choi, S. Jung, K. Chu, D. Jeon, S.-T. Lee, J.H. Kim, S.H. Choi, T. Hyeon, D.-H.

Kim, Nat. Commun. 5 (2014) 5747.

[10] F.-R. Fan, L. Lin, G. Zhu, W. Wu, R. Zhang, Z.L. Wang, Nano Lett. 12 (2012) 3109-3114.

[11] D.J. Lipomi, M. Vosgueritchian, B.C.K. Tee, S.L. Hellstrom, J.A. Lee, C.H. Fox, Z. Bao, Nat. Nano. 6 (2011) 788-792.

[12] C.-C. Kim, H.-H. Lee, K.H. Oh, J.-Y. Sun, Science 353 (2016) 682-687.

[13] C. Larson, B. Peele, S. Li, S. Robinson, M. Totaro, L. Beccai, B. Mazzolai, R. Shepherd, Science 351 (2016) 1071-1074.

[14] Y. Yang, H. Zhang, Z.-H. Lin, Y.S. Zhou, Q. Jing, Y. Su, J. Yang, J. Chen, C. Hu, Z.L. Wang, ACS Nano 7 (2013) 9213-9222.

[15] S. Wang, L. Lin, Z.L. Wang, Nano Energy 11 (2015) 436-462.

[16] S. Chen, B. Zhuo, X. Guo, ACS Appl. Mater. Interfaces 8 (2016) 20364-20370.

[17] D. Kwon, T.-I. Lee, J. Shim, S. Ryu, M.S. Kim, S. Kim, T.-S. Kim, I. Park, ACS Appl. Mater. Interfaces 8 (2016) 16922-16931.

[18] G. Schwartz, B.C.K. Tee, J. Mei, A.L. Appleton, D.H. Kim, H. Wang, Z. Bao, Nat. Commun. 4 (2013) 1859.

[19] Y. Zang, F. Zhang, D. Huang, X. Gao, C.-a. Di, D. Zhu, Nat. Commun. 6 (2015) 6269.

[20] S. Gong, W. Schwalb, Y.W. Wang, Y. Chen, Y. Tang, J. Si, B. Shirinzadeh, W.L. Cheng, Nat. Commun. 5 (2014) 3132.

[21] H. Park, Y.R. Jeong, J. Yun, S.Y. Hong, S. Jin, S.-J. Lee, G. Zi, J.S. Ha, ACS Nano 9 (2015) 9974-9985.

[22] Y.-C. Lai, B.-W. Ye, C.-F. Lu, C.-T. Chen, M.-H. Jao, W.-F. Su, W.-Y. Hung, T.-Y. Lin, Y.-F. Chen, Adv. Funct. Mater. 26 (2016) 1286-1295.

[23] D. Lee, H. Lee, Y. Jeong, Y. Ahn, G. Nam, Y. Lee, Adv. Mater. 28 (2016) 9364-9369.

[24] K. Kim, M. Jung, B. Kim, J. Kim, K. Shin, O.-S. Kwon, S. Jeon, Nano Energy 41 (2017) 301-307.

[25] Z. Lou, S. Chen, L. Wang, K. Jiang, G. Shen, Nano Energy 23 (2016) 7-14.

[26] C. Luo, N. Liu, H. Zhang, W. Liu, Y. Yue, S. Wang, J. Rao, C. Yang, J. Su, X. Jiang, Y. Gao, Nano Energy 41 (2017) 527-534.

[27] B.C.K. Tee, A. Chortos, R.R. Dunn, G. Schwartz, E. Eason, Z. Bao, Adv. Funct. Mater. 24 (2014) 5427-5434.

[28] C.M. Boutry, A. Nguyen, Q.O. Lawal, A. Chortos, S. Rondeau-Gagné, Z. Bao, Adv. Mater. 27 (2015) 6954-6961.

[29] L. Lin, Y. Xie, S. Wang, W. Wu, S. Niu, X. Wen, Z.L. Wang, ACS Nano 7 (2013) 8266-8274.

[30] M.-F. Lin, J. Xiong, J. Wang, K. Parida, P.S. Lee, Nano Energy 44 (2018) 248-255.

[31] B. Wang, C. Liu, Y. Xiao, J. Zhong, W. Li, Y. Cheng, B. Hu, L. Huang, J. Zhou, Nano Energy 32 (2017) 42-49.

[32] C. Pang, G.-Y. Lee, T.-i. Kim, S.M. Kim, H.N. Kim, S.-H. Ahn, K.-Y. Suh, Nat. Mater. 11 (2012) 795-801.

[33] C. Pan, L. Dong, G. Zhu, S. Niu, R. Yu, Q. Yang, Y. Liu, Z.L. Wang, Nat. Photon. 7 (2013) 752-758.

[34] W. Wu, X. Wen, Z.L. Wang, Science 340 (2013) 952-957.

[35] R. Li, Y. Si, Z. Zhu, Y. Guo, Y. Zhang, N. Pan, G. Sun, T. Pan, Adv. Mater. 29 (2017) 1700253.

[36] B. Nie, R. Li, J. Cao, J.D. Brandt, T. Pan, Adv. Mater. 27 (2015) 6055-6062.

[37] A.N. Sokolov, M.E. Roberts, Z. Bao, Mater. Today 12 (2009) 12-20.

[38] M. Kaltenbrunner, T. Sekitani, J. Reeder, T. Yokota, K. Kuribara, T. Tokuhara, M. Drack, R. Schwodiauer, I. Graz, S. Bauer-Gogonea, S. Bauer, T. Someya, Nature 499 (2013) 458-463.

[39] P. Lin, F. Yan, Adv. Mater. 24 (2012) 34-51.

[40] M. Magliulo, K. Manoli, E. Macchia, G. Palazzo, L. Torsi, Adv. Mater. 27 (2015) 7528-7551.

[41] L. Torsi, M. Magliulo, K. Manoli, G. Palazzo, Chem. Soc. Rev. 42 (2013) 8612-8628.

[42] T. Someya, T. Sekitani, S. Iba, Y. Kato, H. Kawaguchi, T. Sakurai, Proc. Natl. Acad. Sci. U.S.A. 101 (2004) 9966-9970.

[43] R.P. Ortiz, A. Facchetti, T.J. Marks, Chem. Rev. 110 (2010) 205-239.

[44] J. Lee, M.J. Panzer, Y. He, T.P. Lodge, C.D. Frisbie, J. Am. Chem. Soc. 129 (2007) 4532-4533.

[45] J.H. Cho, J. Lee, Y. He, B.S. Kim, T.P. Lodge, C.D. Frisbie, Adv. Mater. 20 (2008) 686-690.

[46] L. Herlogsson, Y.-Y. Noh, N. Zhao, X. Crispin, H. Sirringhaus, M. Berggren, Adv. Mater. 20 (2008) 4708-4713.

[47] Z. Zhu, R. Li, T. Pan, Adv. Mater. 30 (2018) 1705122.

[48] Z. Yin, M.-J. Yin, Z. Liu, Y. Zhang, A.P. Zhang, Q. Zheng, Adv. Sci. 5 (2018) 1701041.

[49] S.G. Yoon, S.T. Chang, J. Mater. Chem. C 5 (2017) 1910-1919.

[50] S.G. Yoon, B.J. Park, S.T. Chang, ACS Appl. Mater. Interfaces 9 (2017) 36206-36219.

[51] B. Nie, R. Li, J.D. Brandt, T. Pan, Lab Chip 14 (2014) 1107-1116.

[52] M.L. Jin, S. Park, Y. Lee, J.H. Lee, J. Chung, J.S. Kim, J.-S. Kim, S.Y. Kim, E. Jee, D.W. Kim, J.W. Chung, S.G. Lee, D. Choi, H.-T. Jung, D.H. Kim, Adv. Mater. 29 (2017) 1605973.

[53] S. Jang, E. Jee, D. Choi, W. Kim, J.S. Kim, V. Amoli, T. Sung, D. Choi, D.H. Kim, J.-Y. Kwon, ACS Appl. Mater. Interfaces 10 (2018) 31472-31479.

[54] J.-Y. Sun, X. Zhao, W.R.K. Illeperuma, O. Chaudhuri, K.H. Oh, D.J. Mooney, J.J. Vlassak, Z. Suo, Nature 489 (2012) 133-136.

[55] J. Duan, X. Liang, J. Guo, K. Zhu, L. Zhang, Adv. Mater. 28 (2016) 8037-8044.

[56] J.-Y. Sun, C. Keplinger, G.M. Whitesides, Z. Suo, Adv. Mater. 26 (2014) 7608-7614.

[57] Y. Yang, X. Wang, F. Yang, H. Shen, D. Wu, Adv. Mater. 28 (2016) 7178-7184.

[58] W. Sun, B. Xue, Y. Li, M. Qin, J. Wu, K. Lu, J. Wu, Y. Cao, Q. Jiang, W. Wang, Adv. Funct. Mater. 26 (2016) 9044-9052.

[59] M.j. Yin, Y. Zhang, Z. Yin, Q. Zheng, A.P. Zhang, Adv. Mater. Technol. 3 (2018) 1800051.

[60] M.-J. Yin, M. Yao, S. Gao, A.P. Zhang, H.-Y. Tam, P.-K.A. Wai, Adv. Mater. 28 (2016) 1394-1399.

[61] D. Meinderink, A.G. Orive, G. Grundmeier, Surf. Interface. Anal. 50 (2018) 1-6.

[62] N.S. Samsonova, L.G. Il'chenko, M.M. Gol'dman, L.P. Ni, J. Appl. Spectrosc. 23 (1975) 963-966.

[63] W. Zhang, A.A. Dehghani-Sanij, R.S. Blackburn, Prog. Nat. Sci. 18 (2008) 801-805.

[64] J. Guo, X. Liu, N. Jiang, A.K. Yetisen, H. Yuk, C. Yang, A. Khademhosseini, X. Zhao, S.-H. Yun, Adv. Mater. 28 (2016) 10244-10249.

[65] C. Keplinger, J.-Y. Sun, C.C. Foo, P. Rothemund, G.M. Whitesides, Z. Suo, Science 341 (2013) 984-987.

[66] S.H. Kim, K. Hong, W. Xie, K.H. Lee, S. Zhang, T.P. Lodge, C.D. Frisbie, Adv. Mater. 25 (2013) 1822-1846.

[67] Y. Mao, S. Lin, X. Zhao, L. Anand, J. Mech. Phys. Solids 100 (2017) 103-130.

[68] S.Y. Kim, E. Jee, J.S. Kim, D.H. Kim, RSC Adv. 7 (2017) 23820-23826.

[69] Z. Wang, J. Chen, Y. Cong, H. Zhang, T. Xu, L. Nie, J. Fu, Chem. Mater. 30 (2018) 8062-8069.

[70] T.R.C. Boyde, J. Chromatogr. 124 (1976) 219-230.

[71] Y.D. Park, J.A. Lim, H.S. Lee, K. Cho, Mater. Today 10 (2007) 46-54.

[72] J. Kim, T.N. Ng, W.S. Kim, Appl. Phys. Lett. 101 (2012) 103308.

Ming-Jie Yin received his B.S. degree and M.S. degree in Chemistry from Southwest University and Zhejiang University, China, in 2007 and 2011, respectively. He obtained his PhD degree from The Hong Kong Polytechnic University, China, in 2016 and conducted his postdoctoral research also in the Hong Kong Polytechnic University. His research interests include self-assembly, separation membrane, microfabrication, and novel polymeric materials for sensors.

Zhigang Yin received his Bachelor degree from Xi'an Technological University in 2008 and his Master degree from Fuzhou University in 2011. He then obtained his Ph.D. degree in materials physics and chemistry from University of Chinese Academy of Sciences in 2017. He was a Research Scholar at the Humboldt University of Berlin, Germany since December 2018. He joined the Fujian Institute of Research on the Structure of Matter, Chinese Academy of Sciences (CAS) in 2011, and became an Associate Professor in 2016. His research interests include optoelectronic materials/devices, flexible electronics, and interfacial science.

Yangxi Zhang received his B.S. degree in Microelectronics and B.A. degree in Economics from Peking University in 2010. He obtained his PhD degree in Microelectronics and Solid-State Electronics in 2016 from Peking University. He joined the Hong Kong Polytechnic University as a Postdoctoral Fellow in Department of Electrical Engineering since 2016. His research interests include micro-electro-mechanical systems (MEMS) technology and sensors as well as microfabrication and 3D micro-printing.

Qingdong Zheng received his B.S. degree in fine chemicals and his M.S. degree in applied chemistry from East China University of Science and Technology, China in 1998 and 2001, respectively. He obtained his Ph.D. degree in chemistry from the State University of New York at Buffalo, USA in 2005. After carrying out his postdoctoral research at the Johns Hopkins University, he joined the Fujian Institute of Research on the Structure of Matter, Chinese Academy of Sciences, and became a professor in 2010. His main interests focus on multifunctional molecular materials and devices and in particular on the fields of semiconducting materials and related interfacial materials for photovoltaic applications. He has published more than 100 peer-reviewed papers. He is serving as Associate editor of RSC Advances and as topical editor of Chinese Optics Letters.

A. Ping Zhang received the B.Sc. and M.Sc. degrees from Zhejiang University (ZJU), Hangzhou, China, in 1997 and 2000, respectively, and received the Ph.D. degree from The Hong Kong Polytechnic University (PolyU), Hong Kong, in 2003. He joined the Department of Optical Engineering, ZJU, in 2003 and served as Lecturer and Associate Professor until 2012. He was a Research Scholar of the Institute for Lasers, Photonics, and Biophotonics, State University of New York at Buffalo during the period of 2006–2008, and the Department of NanoEngineering of University of California, San Diego in 2011, respectively. He then joined the Department of Electrical Engineering, PolyU, as an Associate Professor in 2012. His research interests include optical micro-/nano-fabrication technologies, photonic devices, sensors, and microsystem.

Supporting Materials for

Micropatterned elastic ionic polyacrylamide hydrogel for low-voltage capacitive and organic thin-film transistor pressure sensors

Ming-jie Yin[a], Zhigan Yin[b], Yangxi Zhang[a], Qingdong Zheng[b,*], A. Ping Zhang[a,*]

[a] Photonics Research Center, Department of Electrical Engineering, The Hong Kong Polytechnic University, Hong Kong SAR, China

[b] State Key Laboratory of Structural Chemistry, Fujian Institute of Research on the Structure of Matter, Chinese Academy of Sciences, 155 Yangqiao West Road, Fuzhou, China.

*Corresponding author

E-mail address: qingdongzheng@fjirsm.ac.cn (Q. Zheng); azhang@polyu.edu.hk (A.P. Zhang)

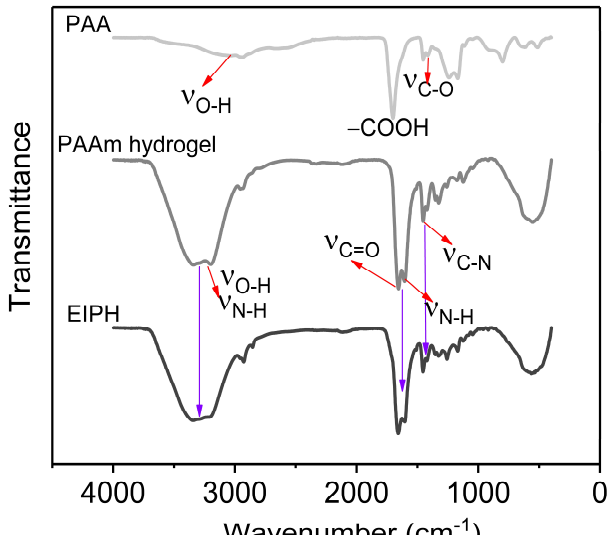

Figure S1. Measured Fourier transform infrared spectroscopy (FTIR) spectra of EIPH, PAA and PAAm hydrogels.

(a)

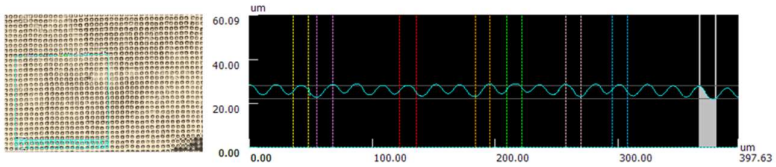

Profile1	Horz. dist.	Hght. diff.	Hght. ave.	Angle	C.S. length	C.S. area
All	397.63um	5.66um	26.06um	0.82°	446.96um	10371.50um2
Seg.1	12.33um	1.13um	27.26um	5.26°	13.45um	345.36um2
Seg.2	13.40um	0.48um	27.25um	2.05°	15.00um	375.79um2
Seg.3	12.33um	1.73um	28.04um	8.01°	13.31um	355.28um2
Seg.4	12.33um	0.27um	27.47um	1.24°	13.86um	348.03um2
Seg.5	13.40um	5.82um	25.65um	23.49°	14.91um	353.74um2
Seg.6	11.25um	5.69um	25.82um	26.83°	12.85um	298.33um2
Seg.7	12.33um	5.70um	25.92um	24.81°	13.92um	328.38um2
Seg.8	12.86um	5.67um	24.32um	23.79°	14.75um	317.25um2

(b)

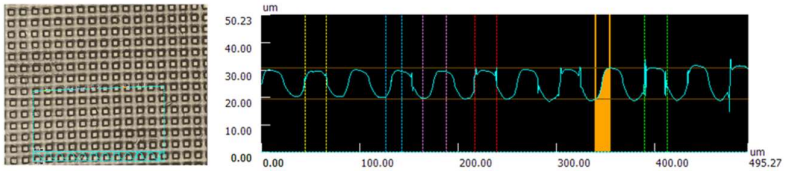

Profile1	Horz. dist.	Hght. diff.	Hght. ave.	Angle	C.S. length	C.S. area
All	495.27um	5.54um	25.43um	0.64°	740.40um	12601.83um2
Seg.1	21.36um	1.58um	29.09um	4.23°	23.55um	628.74um2
Seg.2	22.03um	1.71um	29.22um	4.43°	33.71um	653.28um2
Seg.3	23.36um	3.47um	29.45um	8.44°	92.31um	691.42um2
Seg.4	16.69um	9.45um	26.53um	29.52°	22.56um	454.72um2
Seg.5	23.36um	9.86um	25.18um	22.88°	27.64um	600.67um2
Seg.6	14.68um	11.39um	24.83um	37.81°	20.07um	379.41um2

(c)

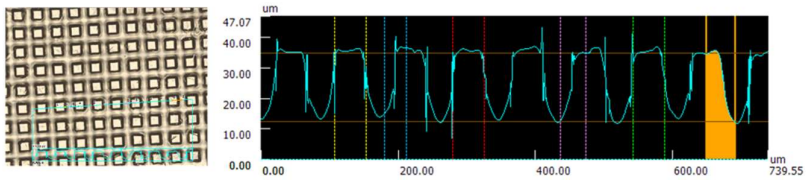

Profile1	Horz. dist.	Hght. diff.	Hght. ave.	Angle	C.S. length	C.S. area
All	739.55um	22.22um	26.62um	1.72°	1503.23um	19702.27um2
Seg.1	44.85um	1.01um	34.98um	1.29°	86.96um	1583.69um2
Seg.2	45.85um	0.32um	34.93um	0.40°	94.54um	1620.42um2
Seg.3	45.85um	8.77um	35.10um	10.83°	58.14um	1628.38um2
Seg.4	30.90um	21.42um	27.68um	34.73°	65.86um	881.83um2
Seg.5	37.87um	22.63um	25.96um	30.86°	60.04um	986.97um2
Seg.6	41.86um	22.35um	27.62um	28.10°	56.31um	1173.19um2

(d)

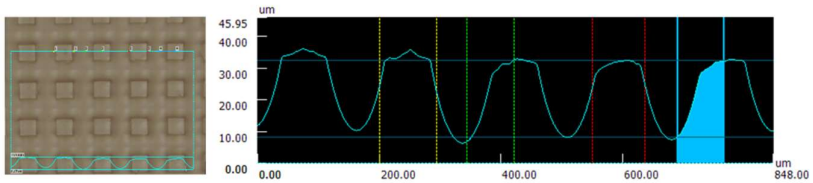

Profile1	Horz. dist.	Hght. diff.	Hght. ave.	Angle	C.S. length	C.S. area
All	848.00um	1.72um	23.14um	0.12°	912.74um	19635.26um2
Seg.1	93.71um	0.76um	32.47um	0.46°	101.46um	3067.09um2
Seg.2	86.86um	2.38um	30.59um	1.57°	91.00um	2667.48um2
Seg.3	76.57um	25.86um	21.82um	18.66°	82.80um	1683.39um2
Seg.4	76.57um	24.11um	22.92um	17.48°	82.34um	1767.99um2

Figure S2. Measured geometric parameters of the EIPH micro-pillar structures. (a) micro-pillars for Sensor-4; (b) micro-pillars for Sensor-3; (c) micro-pillars for Sensor-2; and (d) micro-pillars for Sensor-1.

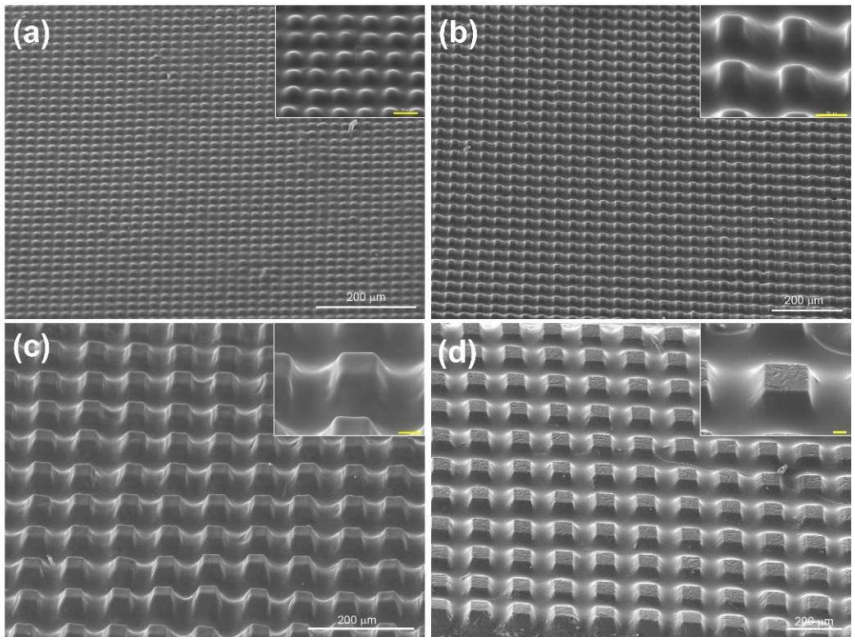

Figure S3. SEM images of the EIPH micro-pillar arrays of different sizes: (a) 10 μm; (b) 20 μm; (c) 40 μm; and (d) 80 μm. The inset shows the enlarged images of EIPH micro-pillar structures, in which the scale bar is 20 μm.

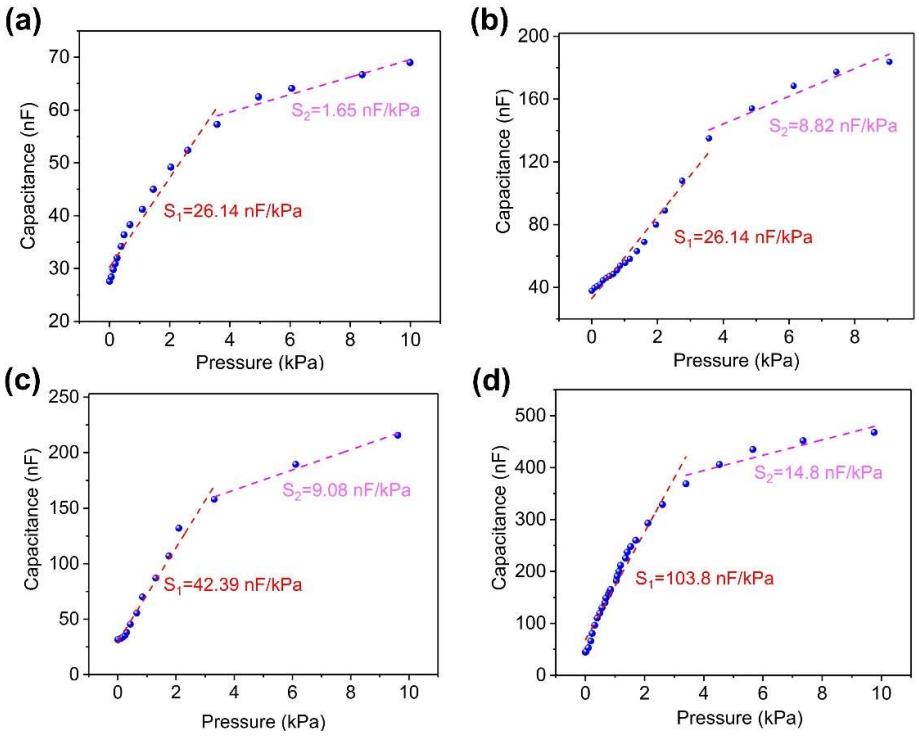

Figure S4. Capacitance (tested at 1 kHz) as a function of applied pressure for the EIPH-based pressure sensors with micropillars of different sizes: (a) Sensor-1: 80 μm; (b) Sensor-2: 40 μm; (c) Sensor-3: 20 μm; and (d) Sensor-4: 10 μm.

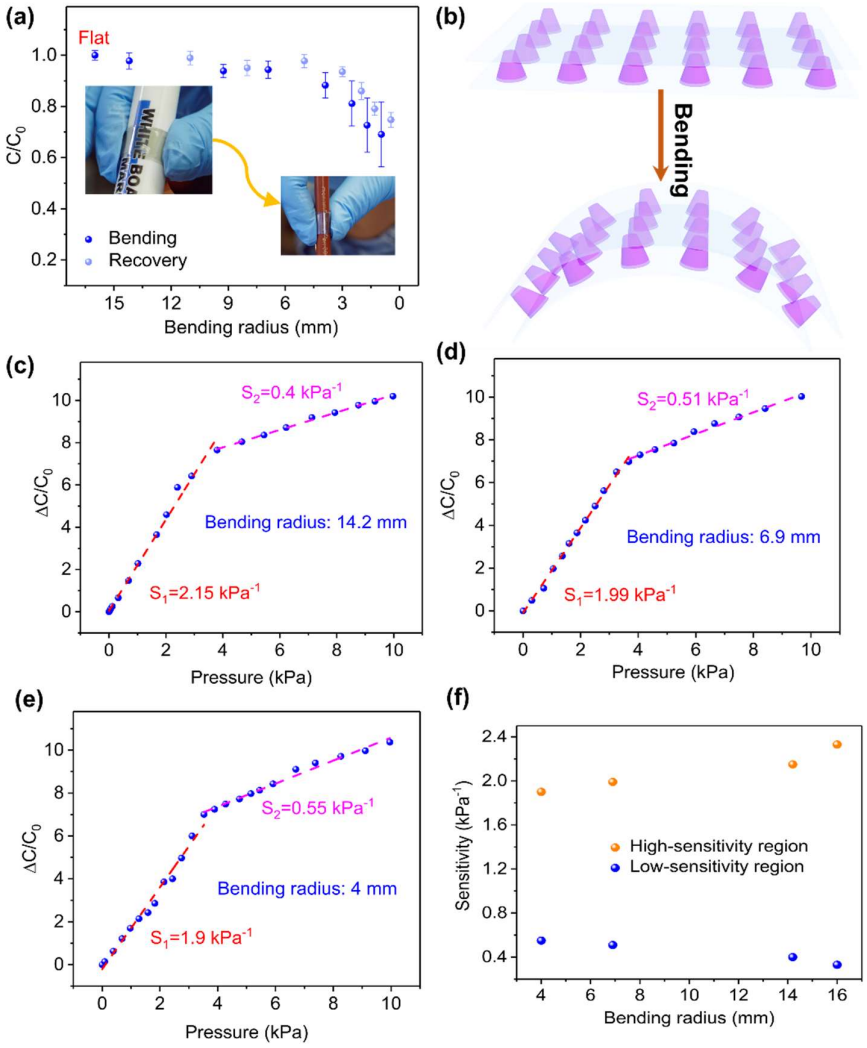

Figure S5. Effects of bending on the pressure sensing performance of Sensor-4. (a) The capacitance changes of Sensor-4 with respect to bending radiuses. (b) Schematic sketch of the microstructure under bending. (c-e) Measured response curves of the Sensor-4 under the bending of different radiuses of curvature: (c) 14.2 mm, (d) 6.9 mm, and (e) 4 mm. (f) Dependence of the sensitivity of Sensor-4 on bending radius.

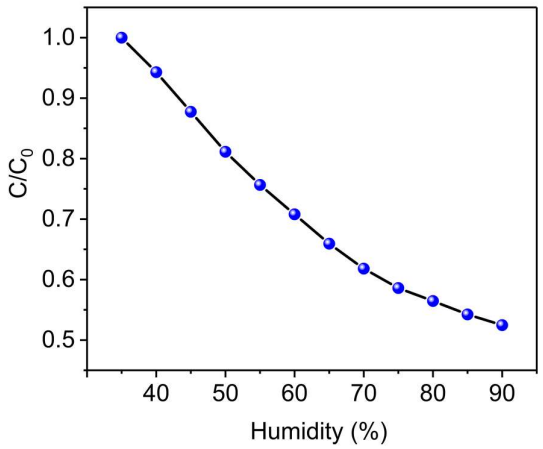

Figure S6. Dependence of the capacitance of the EIPH-based pressure sensor on humidity.

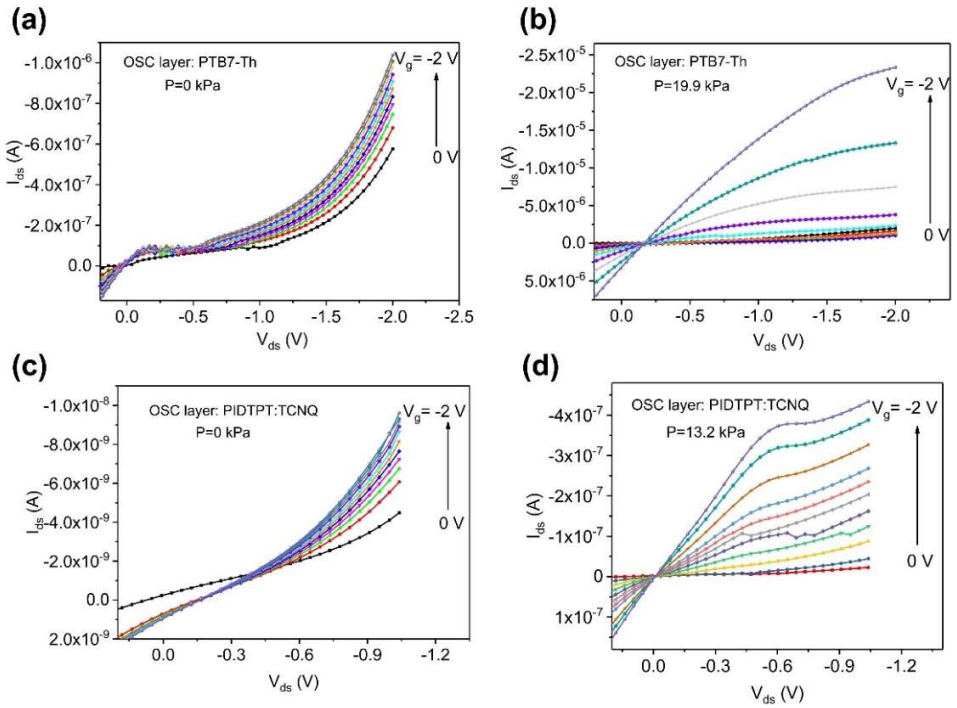

Figure S7. Output curves of two OTFT-based pressure sensors with different OSC layers: (a) PTB7-Th: 0 kPa; (b) PTB7-Th: 19.9 kPa; (c) PIDTBT: TCNQ: 0 kPa; and (d) PIDTBT: TCNQ: 13.2 kPa.

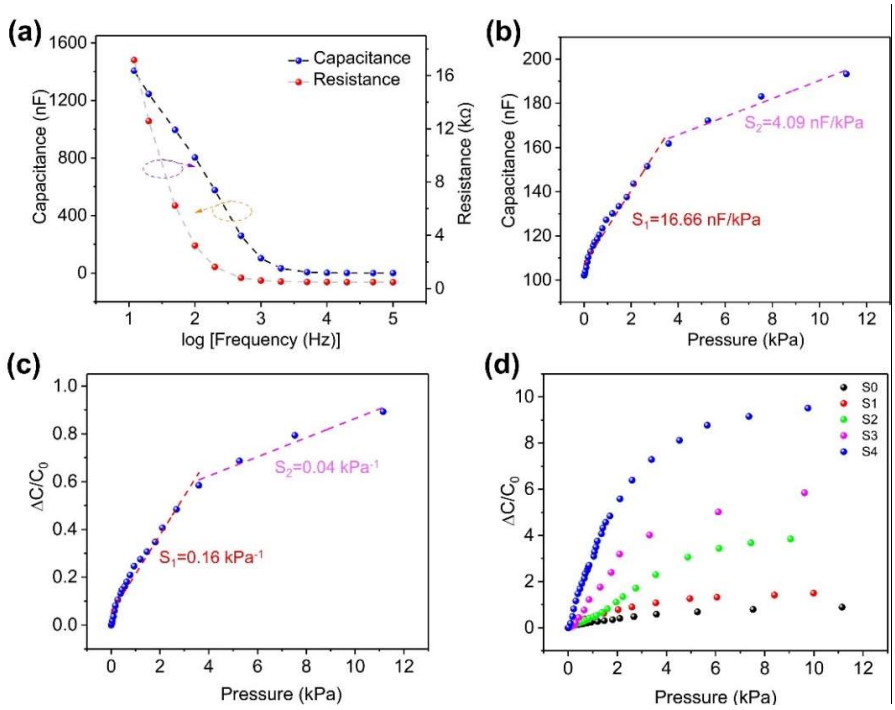

Figure S8. Performance of the capacitive pressure sensor based on the EIPH without microstructures. (a) capacitance and resistance change with measurement frequency; (b) capacitance as a function of applied pressure at 1 kHz; (c) capacitance change to the applied pressure. (d) Summary of performance for all EIPH-based capacitive pressure sensors with and without micro-tower structures.

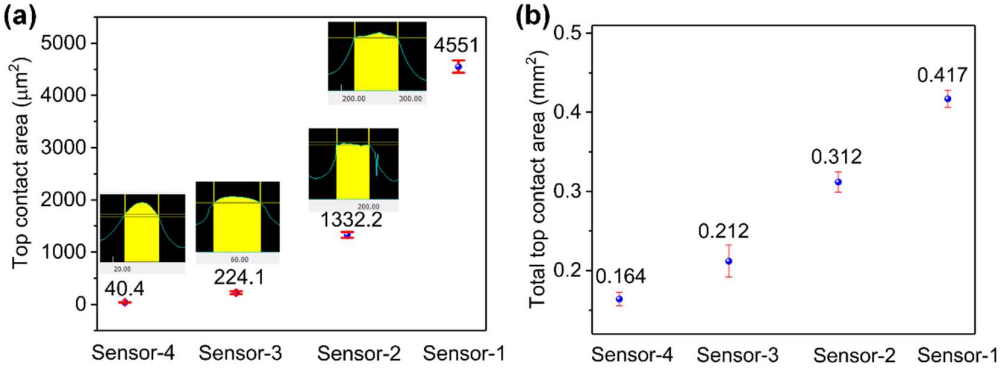

Figure S9. Estimated top contact area of the micropillar (a) and the initial area of the contact between the micropillars and the upper electrode under testing (b). The whole area under test is estimated by the area of the end surface of a round pointed probe, i.e. 1.77 mm^2.